Multiphase Particle-Based Simulation of Poro-Elasto-Capillary Effects

RUOLAN LI*, University of Science and Technology Beijing, China
YANRUI XU*, Tsinghua University, China
YALAN ZHANG, University of Science and Technology Beijing, China
JIRI KOSINKA, University of Groningen, Netherlands
ALEXANDRU C. TELEA, Utrecht University, Netherlands
JIAN CHANG, Bournemouth University, United Kingdom
JIAN JUN ZHANG, Bournemouth University, United Kingdom
XIAOJUAN BAN, University of Science and Technology Beijing, China
XIAOKUN WANG†, University of Science and Technology Beijing, China

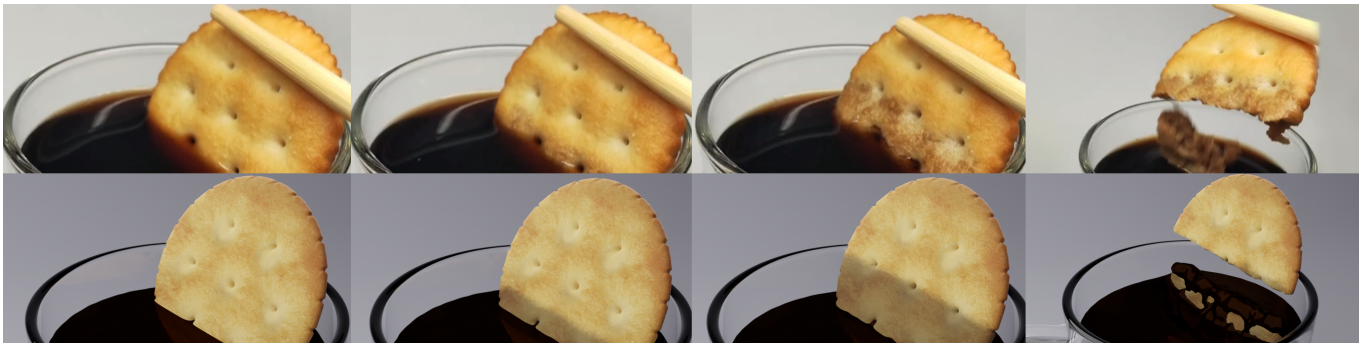

Fig. 1. Comparison between real (top) and simulated (bottom) scenarios: Fracture behavior of a cracker after softening induced by immersion into coffee.

Simulating the interactions between fluids and porous media has attracted significant attention in computer graphics. A key challenge in this domain is modeling the Poro-Elasto-Capillary (PEC) coupling effect which describes the intricate interplay of three physical phenomena in soft porous materials: pore-structure evolution, elastic deformation, and wetting driven by capillary pressure. These phenomena collectively govern dynamic behavior such as the softening and fracturing of biscuits upon water absorption or the swelling of cellulose sponges due to liquid infiltration. Most existing simulation methods model porous media either as static grids or as solid particles with augmented water content attributes, failing to capture the full spectrum of PEC-driven effects due to the lack of physical modeling for elasticity, dynamic porosity changes, and capillary interactions. We propose a multiphase particle-based framework to holistically simulate PEC coupling effects with porous media. We develop a physics-driven model that captures elasticity and dynamic pore-structure evolution under capillary action, enabling realistic simulation of softening and swelling. We derive a saturation-aware pressure Poisson equation to enforce fluid incompressibility within and around the porous medium, ensuring accurate capillary-driven flow while preserving mass and momentum. Finally, we propose a representative elementary volume-based formulation to unify the modeling of homogeneous macro-porous media and cavity-embedded structures, enhancing the representation of pore-scale PEC effects. Comparisons with prior work and real footage show the advantages of our approach in achieving visually realistic fluid-porous media interactions.

CCS Concepts: • **Computing methodologies → Physical simulation**.

Additional Key Words and Phrases: physically-based animation, capillarity, multiphase flow, porous media, incompressible fluid

ACM Reference Format:
Ruolan Li, Yanrui Xu, Yalan Zhang, Jiri Kosinka, Alexandru C. Telea, Jian Chang, Jian Jun Zhang, Xiaojuan Ban, and Xiaokun Wang. 2025. Multiphase Particle-Based Simulation of Poro-Elasto-Capillary Effects. In *SIGGRAPH Asia 2025 Conference Papers (SA Conference Papers '25), December 15–18, 2025, Hong Kong, Hong Kong*. ACM, New York, NY, USA, 11 pages. https://doi.org/10.1145/3757377.3763960

*Both authors contributed equally to this research.
†Corresponding author.

Authors' Contact Information: Ruolan Li, University of Science and Technology Beijing, Beijing, China, dewiorchid2020@gmail.com; Yanrui Xu, Tsinghua University, Beijing, China, xuyanruiedw@me.com; Yalan Zhang, University of Science and Technology Beijing, Beijing, China, yalan.zhang920503@gmail.com; Jiri Kosinka, University of Groningen, Groningen, Netherlands, j.kosinka@rug.nl; Alexandru C. Telea, Utrecht University, Utrecht, Netherlands, a.c.telea@uu.nl; Jian Chang, Bournemouth University, Bournemouth, United Kingdom, jchang@bournemouth.ac.uk; Jian Jun Zhang, Bournemouth University, Bournemouth, United Kingdom, jzhang@bournemouth.ac.uk; Xiaojuan Ban, University of Science and Technology Beijing, Beijing, China, banxj@ustb.edu.cn; Xiaokun Wang, University of Science and Technology Beijing, Beijing, China, wangxiaokun@ustb.edu.cn.

SA Conference Papers '25, Hong Kong, Hong Kong

ACM ISBN 979-8-4007-2137-3/25/12
https://doi.org/10.1145/3757377.3763960

1 Introduction

Porous media are ubiquitous and exhibit a rich array of visual and physical phenomena driven by fluid interactions. Examples include the swelling of cellulose sponges, the softening and fracturing of biscuits upon fluid saturation, and dynamic submersion effects due to the increased weight of wet materials. These fluid-porous interactions are governed by intricate Poro-Elasto-Capillary (PEC) coupling [Ha and Kim 2020; Van de Velde et al. 2023] involving the interplay of fluid flow, elastic deformation, and pore-structure evolution, making their realistic simulation a significant challenge in computer graphics. This complexity further increases for multiphase fluids where interactions between multiple fluid phases and porous structures demand robust physical modeling.

In computer graphics, existing methods for simulating fluid-porous media interactions typically model porous media as static grids or solid particles augmented with water content attributes [Fei et al. 2018; Lenaerts et al. 2008; Su et al. 2023]. Techniques such as Smoothed Particle Hydrodynamics (SPH) or grid-based solvers approximate fluid flow and absorption within porous structures [Patkar and Chaudhuri 2013; Shi and Xiao 2015; Tampubolon et al. 2017; Wang et al. 2024]. Recent approaches incorporate dynamic water content tracking to render wet surfaces and basic deformation [Ren et al. 2021; Yan et al. 2016]. Such methods achieve notable visual results but cannot fully capture the physical complexities of fluid-porous interactions. For instance, grid-based saturation approximations [Fei et al. 2018; Lenaerts et al. 2008] often involve frequent fluid insertion and removal, neglecting granular fluid details within pores, which compromises simulation stability. Yan et al. [2016] incorporated porous solid phases using diffusion-based volume fraction models, which oversimplify fluid representation and lack detailed modeling of pore fluid dynamics. Similarly, Ren et al. [2021] proposed a virtual phase mechanism for multiphase porous flow; their simplified coupling approach compromises mass conservation and incompressibility within the porous medium. Such approaches also struggle with complex, freely moving boundaries, limiting their applicability to dynamic scenarios. This highlights a critical gap in current techniques, as they fail to comprehensively simulate the PEC coupling effects – encompassing pore-structure evolution, elastic deformation, and capillary-driven wetting – that govern diverse phenomena in soft porous materials.

We address these shortcomings by a novel multiphase particle-based framework that holistically simulates PEC coupling effects, supporting both single- and multi-fluid interactions with porous media. We directly tackle the challenges of PEC coupling by modeling the interplay of dynamic pore-structure evolution, elastic deformation, and capillary-driven wetting. We use an elasto-plastic model based on an integral formulation to capture the elasticity and large deformations under wetting, enabling realistic simulations of phenomena like sponge swelling and biscuit softening. By deriving a saturation-aware pressure Poisson equation, we ensure accurate capillary-driven flow while enforcing fluid incompressibility, enhancing the realism of fluid-porous interactions. Additionally, we propose a Representative Elementary Volume (REV)-based formulation to consistently model pore-structure evolution across homogeneous macro-porous media and cavity-embedded structures. An iterative correction method further mitigates abrupt saturation changes, ensuring long-term simulation stability. Our contributions, each addressing a core aspect of PEC coupling, are as follows:

- The first (to our knowledge) multiphase particle-based framework that models the *full spectrum of PEC coupling*, capturing pore-structure evolution, elastic responses to wetting, and capillary-driven flow, enabling realistic simulation of wetting-induced expansion, softening, and fracturing in porous media.
- A *saturation-aware pressure Poisson equation* that enforces incompressibility for fluids within and outside porous structures, ensuring accurate capillary-driven flow while conserving mass and momentum, thus supporting dynamic fluid-porous interactions.
- A *unified REV-based formulation* that enhances pore-scale modeling by consistently representing both homogeneous macro-porous media and intricate cavity-embedded structures, enabling versatile simulation of diverse porous materials under PEC effects.

We start by reviewing related work (Sec. 2). Section 3 presents a detailed exploration of PEC effects. Section 4 describes our approach for modelling the PEC porous flow. We next detail our implementation (Sec. 5), experiments (Sec. 6), and conclusions (Sec. 7).

2 Related work

2.1 Porous media in physics

Porous media are ubiquitous in subsurface geotechnical structures, engineering materials, and biological organisms. Early porous media modeling relied on empirical models, primarily to address hydraulic problems in production processes such as architectural design [Woltmann 1794], as covered in the surveys of Bedford and Drumheller [1983] and De Boer [2012]. Many such physical models remain widely used today. For instance, the Washburn equation [Washburn 1921] is used in many scientific and engineering disciplines to model infiltration dynamics in porous media. Fick's second law [Fick 1855] can be used to describe the permeation and transport of a liquid through homogeneous fabric materials [Das et al. 2007]. Darcy's law [Darcy 1856], derived from seepage experiments, links the velocity of a fluid through a porous medium to the pressure drop, permeability, and viscosity coefficient. Since Darcy's law applies to both homogeneous and heterogeneous porous media, it is widely used in many numerical simulations. Subsequent physical research on porous media has largely focused on adapting and applying these fundamental laws to specific domains [Masoodi and Pillai 2010; Schuchard and Berg 1991]. Notably, the wetting, swelling, and softening dynamics of porous media, such as cookies, exhibit PEC effects that surpass classical capillary theory, attracting widespread attention and prompting research into their underlying physical mechanisms [Ha and Kim 2020; Sweijen et al. 2016; Van de Velde et al. 2023].

2.2 Porous media in graphics

The study of porous behavior has gained significant attention in computer graphics, with applications including cloth, sand, soil, and volumetric solids. Early research on wetting phenomena focused on simulating flow on static planar objects and painting techniques.

Curtis et al. [1997] simulated shallow water flow on paper textiles and handled capillarity by solving a diffusion equation to achieve watercolor effects. Huber et al. [2011] went beyond simple diffusion models by solving Fick's second law, adding a gravity term to simulate liquid absorption in cloth. Lenaerts et al. [2008] introduced a general approach to simulating wetted materials, including cloth and other deformable objects, using SPH to solve Darcy's law within the solid. Rungjiratananon et al. [2008] studied the interaction of fluids with dynamic porous media using SPH to simulate sand, water, and their complex interactions. Yan et al. [2016] extended the above work to include porous media solid phases. Subsequent research has focused on enhancing simulation efficiency and accuracy as well as simulating more complex porous phenomena. Parag et al. [2013] proposed a geometry-based diffusion method for the efficient simulation of internal flow in wetted cloth. Lin et al. [2015] presented a similar pore flow model and combined it with SPH to simulate two-way fluid-hair interactions. Gao et al. [2018] proposed a method to simulate particle-laden flows using a multigrid approach, coupling the fluid and sediment phases through momentum exchange. Fei et al. [2018] modeled the internal flow in fabric porous materials via saturated continuity equations that support anisotropic microstructures. Zheng et al. [2020] explored (im)miscible diffusion models for multi-solvent stains on textiles. Ding et al. [2019] simulated material changes in cooking and baking processes by combining liquid diffusion and gas pressure in a thermodynamic porous model. Ren et al. [2021] proposed a virtual phase mechanism to extend the interaction of fluids with porous media to multiphase flow.

Our unified framework handling multiphase flow and porous media bears similarities to the work of Ren et al. [2021]. Their approach enforces distinct physical constraints on the fluid inside and outside the porous medium by extending the phase fraction formulation. However, while they use *local* physical constraints such as the Navier-Stokes equations, we consistently ensure *global* incompressibility of the fluid, thereby achieving natural mass and momentum conservation. Probst et al. [2024] proposed a unified solver for surface tension and simulated the effects of water absorption and squeezing out water from sponges with defined pore structures. While these methods achieve visual effects, they typically treat porous media as static grids or particles with a water content attribute, failing to capture PEC effects such as the elastic and dynamic pore structure evolution underlying phenomena. Our framework addresses these shortcomings.

3 Poro-Elasto-Capillary Effects

We address the challenge of modeling PEC coupling in soft porous media, focusing on capillary-driven wetting, elastic deformation, and swelling. For a single-phase liquid interacting with a porous medium, penetration depends on wettability, defined by the equilibrium contact angle β via Young's equation

$$\Upsilon \cos\beta = \Upsilon_{sg} - \Upsilon_{sl}, \tag{1}$$

where Υ is the liquid-gas surface tension, Υ_{sg} is the solid-gas interfacial tension, and Υ_{sl} is the solid-liquid interfacial tension. A contact angle $\beta < 90^\circ$ is lyophilic, enabling capillary imbibition.

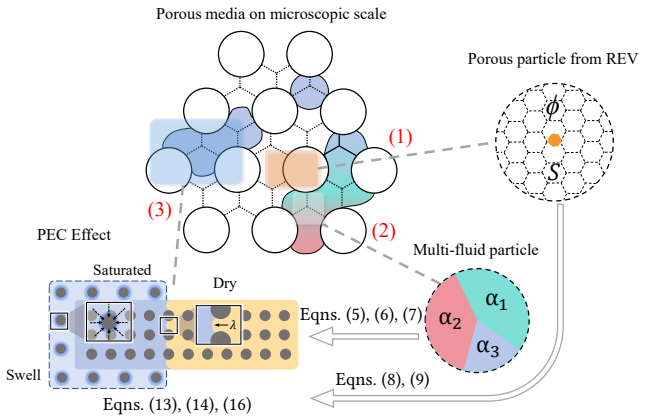

Fig. 2. Our proposed multiphase particle-based framework for porous multiphase flow. We use saturation and porosity attributes to define the REV-based porous particles and compute the associated porous flow behavior (labeled 1). We adapt an implicit mixture model to represent multiphase fluids and extend its governing equations to Darcy flow in porous media (labeled 2), preserving its conservative properties and dynamic accuracy. We account for wetting effects of the porous solid's physical properties using porous and multi-fluid particles to model PEC effects (labeled 3).

Capillary flow is modeled using the Washburn equation, simplified as a capillary with interfacial Laplace pressure given by

$$\Delta p_L = \frac{2\Upsilon\cos\beta}{R}, \tag{2}$$

where R is the capillary radius. For complex pore structures, Darcy's law generalizes fluid flow as

$$\mathbf{q} = -\frac{k}{\eta}\nabla p, \tag{3}$$

where $\mathbf{q}$ is the volumetric flux, k is permeability, η is viscosity, and ∇p is the pressure gradient, driven by Δp_L and external factors.

Figure 2 (lower left) depicts our modeling of capillary wicking and swelling, where soft porous solids (e.g., cellulose sponges) absorb liquid, altering pore structure and causing expansion, where λ denotes the radius of curvature of the leading meniscus. We model this swelling by

$$\sigma = 2G\epsilon + K_{\text{eff}}\phi(S - S_0), \tag{4}$$

where σ is stress, ϵ is strain, S is saturation, S_0 is initial saturation, ϕ is porosity, G is shear modulus, K_{eff} is an effective elastic coefficient, and $\theta = \phi(S - S_0)$ denotes the volumetric strain, which is computed particle-wise as θ_p^{PEC} in our framework (Sec. 4.1). These equations capture the mechanical response to liquid absorption, driving PEC's elastic deformation.

Multiphase flow extends Darcy's law with relative permeability, which is influenced by contact angle and viscosity, enabling PEC coupling across multiple fluid phases.

4 PEC Porous Flow

This section details the technical core of our framework for simulating PEC effects. We begin in **Sec. 4.1** by introducing our fundamental physics-driven model. This section first defines our REV-based particle representation and then presents the governing equations

for saturation, fluid, and solid phases, along with the constitutive models required for their computation. These governing equations provide the foundation for our specific models of the core PEC phenomena detailed in Sec. 3. Subsequently, **Sec. 4.2** details our novel coupling scheme within the pressure solver, which is crucial for handling porous flow while maintaining global fluid incompressibility. Finally, **Sec. 4.3** extends this framework with a microscale sampling method for simulating specific and intricate pore structures, moving beyond the standard REV assumption.

4.1 Physics-Driven Model

Non-equilibrium thermodynamics [de Groot and Mazur 1984] provides the foundation for modeling PEC coupling in soft porous media within the framework of macroscopic continuum mechanics. Our approach captures the dynamic interplay of capillary action, elastic deformation, and pore-structure evolution in porous media. To represent the porous medium across scales, we adopt the concept of a representative elementary volume (REV) [Hassanizadeh and Gray 1990] which comprises a set of pores (see Fig. 2, labeled 1). Kjelstrup et al. [2018] noted that this REV construction is analogous to the methodology in SPH, enabling a unified representation of homogeneous and heterogeneous systems. In our framework, each porous particle physically corresponds to a REV, facilitating the simulation of PEC effects such as saturation-driven expansion and softening. For convenience, all notations of our PEC framework further used in this paper are listed in Tab. 1.

Saturation Dynamics and Governing Equations. The saturation S_k of phase k in the porous medium represents the volume fraction of that phase within the pore space. S_k influences capillary action and the evolution of the pores structure in PEC coupling. The total volume fraction of fluid phases satisfies

$$\sum_k (S_k + R_k) = \sum_k \alpha_k = 1, \tag{5}$$

where R_k is the residual volume fraction (total fluid volume fraction minus the absorbed fraction), and α_k denotes the volume fraction of phase k within the mixture particle. Saturation evolves according to the transport equation

$$\frac{DS_k}{Dt} = \frac{q_k}{\phi\rho_k} - \frac{\nabla\cdot(\rho_k \mathbf{v}_k^D)}{\phi\rho_k} + \mathbf{v}_k\cdot\nabla S_k, \tag{6}$$

where the material derivative $\frac{D}{Dt} \equiv \frac{\partial}{\partial t} + \mathbf{v}_k\cdot\nabla$ describes the time rate of change following phase k motion; q_k is the Darcy flux source, which encapsulates capillary effects central to PEC coupling. The rest density ρ_k and velocity $\mathbf{v}_k$ describe phase k. The Darcy velocity, which is the apparent seepage velocity of fluid phase k in the porous medium, is given by $\mathbf{v}_k^D = -\frac{k}{\eta}\kappa(\phi)\nabla p_k$. Here, $\kappa(\phi)$ is the permeability variation factor, related to porosity ϕ. In SPH, particle motion implicitly handles advection, eliminating the explicit term. This equation governs saturation changes that drive the PEC effect and will be computed using the Darcy flux.

Constitutive Models for Fluid and Solid Phases. To capture the volume fraction occupied by the fluid and account for its dynamic impact on the physical properties of the porous medium, let $S_{p,k}$ be the saturation of the porous solid particle p of phase k; and let $S_{f,k}$ be the saturation of fluid particle f of phase k. The fluid phase k then obeys the momentum conservation equation

$$\alpha_k\rho_k\frac{D\mathbf{v}_k}{Dt} = \alpha_k\left(-\nabla p_k + \nabla\cdot\boldsymbol{\tau}_k + \rho_k\mathbf{g}\right) + \mathbf{M}_k^I + \mathbf{M}_k^D, \tag{7}$$

where p_k, $\boldsymbol{\tau}_k$, $\mathbf{g}$ are the pressure, viscous stress tensor, and gravity, resp.; $\mathbf{M}_k^I$ is the interphase momentum source; and $\mathbf{M}_k^D$ is is the Darcy source term proposed in our work (extending [Xu et al. 2023]'s formulation) which accounts for the influence of the porous medium on the multiphase flow particles. This influence covers effects such as capillary forces and pore-scale forces. Accordingly, the Darcy phase momentum source for fluid particle f is defined as

$$\mathbf{M}_{f,k}^D = \underbrace{\psi_c\rho_k S_{f,k}\sum_{f_p}\left(1 - S_{f_p,k}\right)\frac{m_{f_p}}{\rho_{f_p}}\nabla W_{f\leftarrow f_p}}_{\boldsymbol{M}_k^{\text{cap}}} + \underbrace{\psi_{st}S_{f,k}\mathbf{v}_k\frac{m_f}{V_f^0}}_{\boldsymbol{M}_k^{\text{pore}}}, \tag{8}$$

where $\boldsymbol{M}_k^{\text{cap}}$ is the capillary momentum source [Hilfer 2006]; $\boldsymbol{M}_k^{\text{pore}}$ is the pore momentum source [Slattery 1969]; ψ_c and ψ_{st} are intensity factors (empirically set to 0.02 in our work); m_f and V_f^0 are the mass and rest volumes of fluid particle f; m_{f_p} and ρ_{f_p} are the mass and density of neighboring porous particle f_p, resp.; and $\nabla W_{f\leftarrow f_p}$ is the gradient of the SPH cubic spline smoothing kernel [Ihmsen et al. 2014] centered at f and evaluated at f_p. We use the same notation $X_{a\leftarrow b}$ to indicate the effect of a particle b on particle a's quantity X. The summation over f_p is over all fluid particles.

For the solid phase, we use a peridynamics-based elastoplastic model [Chen et al. 2018], leveraging its integral nature for enhanced stability over traditional SPH methods, especially in scenarios with

Table 1. Key notations for PEC coupling.

Symbol	Domain	Description
α_k	Fluid	Phase k volume fraction
$S_{f,k}$	Fluid	Saturation of fluid particle f for phase k
R_k	Fluid	Residual volume fraction of phase k
q_k	Fluid	Darcy flux source for phase k
$q_{f,k}$	Fluid	Darcy flux of phase k for fluid particle f
$\mathbf{M}_{f,k}^D$	Fluid	Darcy phase momentum source for fluid particle f
$p_{f,k}^0$	Fluid	Rest fluid pressure for phase k of fluid particle f
$\boldsymbol{F}_{f\leftarrow f_p}^p$	Fluid	Pressure force from porous solid neighbor f_p on f
V_R	Fluid	Residual fluid volume
k	Porous	Permeability of the porous medium
$\kappa(\phi)$	Porous	Permeability variation factor
ϕ	Porous	Porosity of the porous medium
ϕ_p	Porous	Porosity of particle p in microscopic modeling
$S_{p,k}$	Solid	Saturation of solid particle p for phase k
$\mathbf{T}_{p\leftarrow p_p}$	Solid	Elastic internal force on particle p by neighbor p_p
θ_p	Solid	Dilation of solid particle p
p_p^D	Solid	Pore pressure within solid particle p
p_0	Solid	Static pore pressure
V_{p_p}	Solid	Volume of neighboring solid particle p_p
$\boldsymbol{F}_{p\leftarrow p_f}^p$	Solid	Pressure force from fluid neighbor p_f on p
ψ_c	Parameter	Intensity factor for capillary momentum source
ψ_{st}	Parameter	Intensity factor for pore momentum source
a_p	Parameter	Saturation-dependent material parameter
b_p	Parameter	Saturation-dependent material parameter
ϵ_k^s	Parameter	Softening coefficient for phase k
ϵ_k^e	Parameter	Dilation coefficient for phase k
$\varkappa$	Parameter	Porosity change factor

large deformations and fracture. The elastic internal force $\mathbf{T}_{p\leftarrow p_p}$ exerted on solid particle p by its solid neighbor p_p is defined as

$$\mathbf{T}_{p\leftarrow p_p} = \frac{1}{2}\tilde{r}\left[4wa_p\tilde{r}\cdot\tilde{r}_0\theta_p + 4wb_p\left(\eta^d - \eta^p\right)\right], \tag{9}$$

where $\tilde{r} = \frac{\mathbf{r}}{\|\mathbf{r}\|}$; $\mathbf{r} = \mathbf{x}_p - \mathbf{x}_{p_p}$; $w = \frac{h}{\|\mathbf{r}\|}$; h is the kernel support; $\tilde{r}_0$ equals $\tilde{r}$ in the rest configuration; η^d and η^p are the deviatoric and plastic displacements resp.; and θ_p quantifies dilation. The detailed derivation can be found in Chen et al. [2018].

Darcy Flux Computation. To compute the saturation changes in (6), we calculate the Darcy flux q_k for each particle f as

$$q_{f,k} = -\frac{k}{\eta}\kappa(\phi)\sum_{f_p}\left(\alpha_{f,k} - S_{f,k} + S_{f_p,k}\right)\nabla p_{f,k}. \tag{10}$$

The pressure gradient $\nabla p_{f,k}$ in (10) is computed as

$$\nabla p_{f,k} = \sum_{f_p} V_p\left(p^D_{f_p} - p^0_{f,k}R_{f,k}\right)\nabla W_{f\leftarrow f_p}, \tag{11}$$

where V_p is the volume of solid particle p, $p^0_{f,k}$ is the rest fluid pressure for k phase of fluid particle f, and $p^D_{f_p}$ is the pore pressure of the solid particle f_p as neighbor of fluid particle f. We compute the pore pressure p^D_p of particle p within the solid as

$$p^D_p = p_0\sum_k S_{p,k} - \theta_p M, \tag{12}$$

where p_0 is the static pore pressure (typically 1000 in our simulations), M controls pore compressibility, and θ_p is the dilation.

PEC Effect Mechanism. To capture PEC-driven phenomena like softening and swelling upon wetting (see Sec. 3), we define the material parameters a_p and b_p in (9) as

$$a_p = a_0\sum_k \epsilon^s_k S_{p,k}, \quad b_p = b_0\sum_k \epsilon^s_k S_{p,k}, \tag{13}$$

where a_0 and b_0 are determined by the initial bulk and shear moduli [Chen et al. 2018], resp., and ϵ^s_k is a softening factor. This models the softening dynamics under PEC, as described by (4), in our framework. The dilation θ_p in (9) is given by

$$\theta_p = \underbrace{\frac{9}{4\pi h^3}\sum_{p_p}\left(\frac{\|\mathbf{r}\|}{\|\mathbf{r}_0\|} - 1\right)V_{p_p}}_{\theta^0_p} + \underbrace{\sum_k \epsilon^e_k S_{p,k}}_{\theta^{\mathrm{PEC}}_p}, \tag{14}$$

where $\mathbf{r}_0$ represents $\mathbf{r}$ in the rest configuration; ϵ^e_k is the dilation factor; V_{p_p} is the volume of the neighbor particle p_p of p. θ^0_p is the initial value of dilation. The second term θ^{PEC}_p is how our framework models the wetting-induced swelling strain under the PEC effect.

Finally, we model the pore evolution process under PEC. Let $\kappa(\phi)$ be the permeability variation factor, which can be described by the Kozeny-Carman equation [Chen et al. 2006] as

$$\kappa(\phi) = \frac{\phi^3(1-\phi_0)^2}{\phi_0^3(1-\phi)^2}, \tag{15}$$

where ϕ_0 is the rest porosity. The relationship between the permeability of a porous medium and its porosity is next

$$\phi = \min\left(1, \phi_0 e^{\varkappa\left(p^D_p - p_0\right)}\right), \tag{16}$$

where $\varkappa$ is the porosity change factor. The change in porosity is dependent on the change in pore pressure and is clamped within the range $[0, 1]$.

4.2 Coupled Dynamics of Residual Fluid

Upon absorption, fluid within the porous medium ceases collisional repulsion with the solid, unlike the remaining external fluid. Regardless of absorption, all fluid adheres to the Navier-Stokes equations, keeping incompressibility and collision-free boundary interactions.

The harmonic averaging approach of Ren et al. [2021] suffers from limitations in complex configurations, fails to fully enforce Navier-Stokes within porous media, and shows instability under large volume changes. Our boundary-particle-based coupling framework offers superior handling of residual fluid interactions, enabling complex *free* boundaries while obeying Navier-Stokes and fluid incompressibility both inside and outside the porous medium.

Consistent with Xu et al. [2023], we use volume incompressibility, which is better suited for multiphase flows with non-uniform densities. To enforce incompressibility while accounting for potential overlap, we adapt the iterative pressure solver from Divergence-Free SPH (DFSPH) [Bender and Koschier 2016]. This approach is equivalent to solving a pressure Poisson equation to find pressures that prevent density fluctuations. The resulting saturation-aware pressure forces are given by:

$$\boldsymbol{F}^p_{f\leftarrow f_p} = -\frac{\kappa^v_f}{\gamma_f}(V_R)^2\sum_{f_p} V^0_{f_p}\nabla W_{f\leftarrow f_p} - V_R\sum_{f_p}\frac{\kappa^v_{f_p}}{\gamma_{f_p}}\left(V^0_{f_p}\right)^2\nabla W_{f\leftarrow f_p}, \tag{17a}$$

$$\boldsymbol{F}^p_{p\leftarrow p_f} = -\frac{\kappa^v_p}{\gamma_p}\left(V^0_p\right)^2\sum_{p_f} V_R\nabla W_{p\leftarrow p_f} - V^0_p\sum_{p_f}\frac{\kappa^v_{p_f}}{\gamma_{p_f}}(V_R)^2\nabla W_{p\leftarrow p_f}, \tag{17b}$$

where κ^v is the DFSPH stiffness coefficient and γ is the local compression state. Summations f_p and p_f go over all fluid, respectively porous solid, particles. The compressibility of particle i can be written as $\gamma_i = \sum_j V^0_j W_{ij}$. $\mathcal{L} = k/\eta$ is the mobility ratio. Using the tight correlation between permeability and residual fluid volume changes, we compute the residual fluid volume as

$$V_R = V^0_f\sum_k \frac{R_k}{\mathcal{L}_k + 1}. \tag{18}$$

In the saturation-aware Poisson-derived pressure solution (Eq. (17)), the effective volume change of fluid entering the solid under capillary wetting is considered (used solely for pressure). Absorbed fluid no longer contributes to collisions, but fluid particle interactions retain their original volume, ensuring global incompressibility, mass, and momentum conservation. This consistent volume treatment for all particles, including boundaries, provides a robust foundation for PEC coupling and enhances adaptability to complex boundaries.

4.3 Microscale Pore-Specific Sampling Modeling

In REV, we can assume an extreme case where the porosity is 1, meaning the porous medium consists entirely of cavities. Therefore, we can perform particle-based modeling for porous media with specific cavity structures. Inspired by morphological approaches to pore-scale modeling of porous media, particularly using maximal inscribed spheres for pore space morphology analysis [Silin and

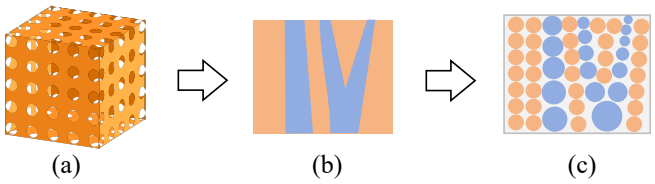

Fig. 3. Microscale pore structure modeling. (a) Representative medium; (b) Extracted capillary structures (orange solid, blue cavity); (c) Pore-adaptive particle sampling.

Patzek 2006; Silin et al. 2003], we use a modified porous particle method for sampling specific pore structures (see Fig. 3). Our sampling method can capture microscale capillary effects within the porous structure, allowing the fluid to be drawn into the porous medium against gravity, consistent with the capillary-driven wetting mechanism in PEC coupling.

We first sample the pore space distribution using particles. Based on the principle of capillary action, the thinner the capillary tube, the higher the rise of fluid. We estimate tube thickness by the local density of particles: the more neighbors a particle has, the thicker the tube, hence lower capillarity. In detail, we estimate porosity from the capillary effect intensity coefficient at pore particle p as

$$\phi_p = c\phi_0 / \sum_{p_p} W_{p \leftarrow p_p}, \tag{19}$$

where c is a coefficient regulating porosity. The capillary pressure can be obtained using the Leverett J-function [1941] which unifies the capillary force curves

$$P_c(S_p) = 2\zeta \sqrt{\frac{\phi_p}{k}} J(S_p), \tag{20}$$

where ζ is the surface tension coefficient and $S_p = \sum_k S_{p,k}$. By replacing $p_0 \sum_k S_{p,k}$ in the pore pressure equation (12) with $P_c(S_p)$, we derive the pore-scale pressure within the porous medium, consistent with PEC's capillary-driven dynamics.

5 Implementation

We integrate DFSPH [Bender and Koschier 2016] into our multiphase particle PEC framework. Algorithm 1 shows our workflow. Our implementation is open source for replicability [Li 2025].

5.1 Adaptive Dynamic Porous Parameters

We compute the contributions $C_{f,k}$ (from solid particles near fluid ones) and $C_{p,k}$ (from multiphase fluid particles near solid ones) as

$$C_{f,k} = \sum_{f_p} W_{f \leftarrow f_p}, \qquad C_{p,k} = \sum_{p_f} \alpha_k W_{p \leftarrow p_f}. \tag{21}$$

To model *multiple* porous media with varying properties interacting with a fluid, the effective permeability should depend on both the porous medium and the fluid. For this, (10) computes permeability on-the-fly based on the current interacting fluid and porous medium. Consider a fluid particle surrounded by porous solid particles with different permeabilities within a heterogeneous medium. To obtain the fluid's permeability, we interpolate from the permeabilities of the neighboring solid particles via

$$k_{f,k} = \sum_{f_p} \sum_{k} \frac{k_{f_p,k} W_{f \leftarrow f_p}}{C_{f,k}}. \tag{22}$$

This approach enables accurate representation of permeability and related properties even when the porous medium exhibits spatial heterogeneity. The saturation of the porous solid is computed using

$$S_{p,k} = \frac{1}{\rho_k V_p^0} \sum_{p_f} \frac{S_{p_f,k} m_f \rho_k W_{p \leftarrow p_f}}{\rho_m C_{p,k}}, \tag{23}$$

where the mixture density is given by $\rho_m = \sum_k \alpha_k \rho_k$.

5.2 Handling Abrupt Variations in Residual Volume

While phase transfer mechanisms within multiphase flows may seem unproblematic in isolated scenarios, they can introduce challenges in complex coupled porous media environments. Differential phase drift velocities in multiphase flows transport phase fractions, but within porous media, this can lead to a significant increase in the phase fraction of a fluid that, due to its initially low residual saturation, was minimally influenced by repulsive forces. This process may increase the effective volume of a less permeable phase, as described by (18), causing 'ejection' artifacts by a sudden rise in the repulsive force exerted by the solid matrix on fluid particles.

We address this issue through an iterative procedure for computing phase fraction changes within the porous framework. We first predict transported phase fractions. For each multiphase flow particle, we verify two conditions: (1) the sum of phase fractions is non-negative; and (2) saturation changes remain within a threshold. This ensures mass conservation and prevents spurious particle ejection artifacts. Particles failing to meet these criteria are flagged, and their scaling factor (a correction coefficient ranging 0-1 that adjusts inter-particle fluxes) in subsequent iterations is set to zero, following the approach in [Jiang and Lan 2021]. The phase fraction transport values for the current time step are determined once all particles satisfy these conditions. Figure 4 shows this correction prevents spurious particle ejections and maintains stability.

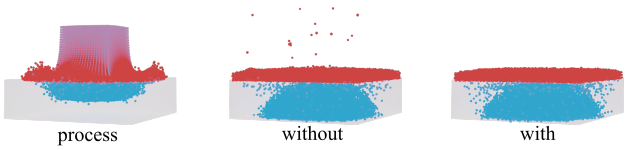

Fig. 4. Ablation experiment for Sec. 5.2. (Left) Initial: two-phase fluid poured onto porous medium. Cyan phase absorbs while red phase is repelled. (Middle) Without correction: abrupt saturation changes cause artifacts. (Right) With correction: stable simulation and smooth phase separation.

6 Experiments

We implemented our framework using Taichi [Hu et al. 2019]. All experiments were performed on an NVIDIA 3090 Tensor Core GPU, with visualizations rendered in Blender's Cycles engine. Experimental setup and parameters are detailed in Tab. 2. See the supplementary video for additional results.

Algorithm 1: Multiphase PEC Simulation per Time Step

for each fluid particle f **do**	//fluid advection
Compute fluid velocity by gravity and viscosity	
for each particle **do**	//compute porous flow quantities
Compute p_p^D for solid and $\nabla p_{f,k}$ for fluid	Eqns. (12), (11)
Compute $q_{f,k}$ and update $S_{f,k}$ for fluid	Eqns. (10), (6)
Compute $\mathbf{M}_{f,k}^D$ and $\mathbf{v}_k$ for fluid	Eqns. (8), (7)
for each porous solid particle p **do**	//PEC effects calculation
Compute a_p, b_p and θ_p for porous particles	Eqns. (13), (14)
Update porosity ϕ	Eqn. (16)
Compute $\mathbf{T}_p$ for porous particles	Eqn. (9)
Update solid velocity by gravity and viscosity	
for each particle **do**	//compute pressure force and update position
Compute $\boldsymbol{F}_f^p$ for fluid and $\boldsymbol{F}_p^p$ for solid	Eqns. (17), (18)
Update all particle positions $\mathbf{x} \leftarrow \mathbf{x} + \mathbf{v}\Delta t$	

6.1 Direct Manifestation of PEC Effects

We explored the behavior of porous materials under wetting effects. Figure 1 shows the capillary-driven penetration of coffee into a cracker, followed by the fracture of the softened, wetted lower part of the cracker when lifted, attributed to the PEC effect. A comparison with photographs of the actual real-world scenario qualitatively validates our method. Figure 5 demonstrates the gradual swelling of a sponge-like solid as it absorbs water from a block placed on its right side, showcasing our model's ability to capture fluid-porous solid interactions.

A direct comparison based on the original experiment from [Ren et al. 2021] (Figure 6) reveals our method's superior capability in capturing realistic poroelastic swelling.

Figure 7 compares swelling effects in a different scenario. [Ren et al. 2021] achieves wetting-induced swelling via stress tensor changes, but the effect is minimal. Our approach exhibits distinct volumetric expansion of the porous solid post-wetting. By comparing the wetting-induced swelling strain with a real-world observation of a cellulose sponge, our results demonstrate closer agreement.

In Fig. 8, a sponge plug initially rests in a funnel. Upon fluid introduction, the plug in the right image softens due to wetting and slips through the funnel, while the plug in the left image retains rigidity and allows complete drainage. This highlights variable softening behavior controlled by wetting dynamics.

Figure 9 examines selective absorption effects. A porous rabbit in a funnel remains stiff when exposed to a low-absorption blue fluid but softens with a high-absorption red fluid, passing through the funnel. These results demonstrate phase-specific interactions.

In Figure 10, a doughnut-shaped biscuit is immersed in a water-filled bowl. Due to high absorption and permeability, the biscuit rapidly absorbs water, altering its Young modulus. When removed and subjected to tensile forces, the dry upper section, unaffected by wetting, exhibits a clean break, while the softened lower section fractures into multiple segments. Secondary fracturing occurs as fragments fall to the bowl's bottom, forming small pieces. The simulation remains stable throughout its entire time range.

6.2 Capillary-Driven Fluid Dynamics in PEC

Figure 11 highlights differences in simulating permeability effects. The method of [Yan et al. 2016], which relies on phase fraction diffusion to model permeability, lacks a detailed representation of fluid behavior within porous materials and requires additional effort to be added to achieve visual mass conservation. In contrast, our method demonstrates clear fluid absorption into the porous solid, as evidenced by the final liquid surface height. Compared to the real-world scenario of fluid infiltration into a sponge, our method similarly exhibits a distinct and observable fluid infiltration boundary, making it more physically accurate and more closely aligned with reality.

Figure 12 shows the dynamic behavior of a porous duck in water. Initially impermeable and less dense than water, the duck floats. Making the duck permeable next causes gradual water absorption, increasing weight, submerging partially, and shifting its center of gravity. Eventually, the duck saturates completely and sinks to the floor. Unlike prior methods [Ren et al. 2021], which artificially increase particle mass to obtain this effect, our approach achieves this naturally, also ensuring mass and momentum conservation.

Figure 15 demonstrates a four-phase miscible fluid flowing through porous filter layers, each absorbing a specific phase, leaving only the blue fluid phase unfiltered. The three layers sequentially absorb the red, yellow, and green phases. Distinct multiphase fluid permeabilities enable selective absorption for each layer.

In Figure 16, a kitchen sponge scenario is simulated. A dry sponge placed in a sink absorbs water from a running faucet, diffusing moisture until saturation. When picked up and twisted at both ends, the sponge expels a portion of the absorbed water.

Figure 17 depicts a microscale porous solid (gray) absorbing the fluid (beige) through capillary action. The fluid overcomes gravity, permeating the pore network. Eventually, the fluid level internal surpasses the external fluid level, simulating capillary effects.

6.3 Numerical Validation

Figure 13 compares our method with [Ren et al. 2021] both visually and quantitatively. our method maintains fluid incompressibility both inside and outside porous media as shown by the near-zero compression ration in the right chart, which represents the average deviation from the uncompressed state ($\gamma_i - 1$) across all fluid particles. In contrast, [Ren et al. 2021] achieves incompressibility only outside the porous medium, with notable compression inside. The inherent mass conservation arising indirectly from incompressibility ensures that in the experiment shown in Fig. 12 the porous duck naturally sinks after water absorption without any artificial mass augmentation.

The chart also compares computational performance. Initially, our method shows higher runtime (solid blue line) due to rapid fluid absorption creating more particle neighbors and increasing search costs. As simulation progresses, the [Ren et al. 2021] runtime (solid orange line) surpasses ours, likely due to computational challenges from highly compressed particle states.

This reflects a characteristic of our method. When conditions are stable and solid models are identical, our efficiency is comparable

Table 2. Experiment configurations.

Scene	Figure	Particle count	Particle size [m]	Permeability k	ϵ_e^s	ϵ_k^s	Δt	Sec./frame
Cracker	Fig. 1	1.26M	0.022	2	0	1	4.4×10^{-4}	12.936
Swell	Fig. 5	805K	0.03	3	0.9	1	6.0×10^{-4}	4.298
Plug	Fig. 8	578K	0.05	6	0	0.05	1.0×10^{-3}	3.566
Bunny	Fig. 9	283K	0.04	0, 10	0, 0	1, 1	8.0×10^{-4}	1.18
Cookie	Fig. 10	658K	0.02	10	0	0.05	4.0×10^{-4}	7.51
Duck	Fig. 12	644K	0.04	3	0	0.05	8.0×10^{-4}	4.053
Phase absorb	Fig. 15	770K	0.04	0, 5, 10	0	1	8.0×10^{-4}	4.236
Wring	Fig. 16	504K	0.02	3	0	1	4.0×10^{-4}	3.882
Specific	Fig. 17	1.17M	0.025	5	0	1	5×10^{-4}	6.682

to [Ren et al. 2021]. Porous coupling adds approximately 15% runtime compared to standard fluid-solid interaction. However, this overhead grows with the number of absorbed fluid particles.

Figure 14 shows a continuous fluid injection into a high-permeability porous medium, presenting both a visual sequence and a quantitative plot of system kinetic energy and momentum. Visually, our method remains stable throughout the simulation, while [Ren et al. 2021] suffers from particle boundary penetration and instability in this long-duration scenario. This observation is quantitatively confirmed by the kinetic energy and momentum plot. During fluid injection, both methods show initial energy increases. However, after injection ceases, our system's energy and momentum smoothly dissipate and converge to a steady state, as expected. In contrast, the energy curve for [Ren et al. 2021] exhibits spurious oscillations and fails to stabilize, and its momentum does not drop to the expected near-zero value. While this setup is not a strict conservation test due to external forces and viscous effects, our method demonstrates superior robustness and momentum preservation. This aligns with the theoretical momentum-conserving properties of our multiphase flow and elasto-plastic formulations [Madenci and Oterkus 2014; Xu et al. 2023], which our coupling framework preserves.

A qualitative comparison between the desirable features of porous media simulation covered by our work, [Ren et al. 2021], and [Yan et al. 2016] is shown in Tab. 3.

7 Conclusion

We have presented a multiphase particle-based framework to address the challenge of modeling PEC coupling in soft porous media, focusing on the interplay of capillary-driven wetting, elastic deformation, and material softening. Our method centers on a saturation-aware pressure Poisson equation, which ensures fluid incompressibility and conserves mass and momentum, thereby providing a stable and robust numerical foundation for PEC simulations. Additionally, a REV-based formulation integrates macro- and micro-scale porous structures, extending the scope of PEC modeling to encompass detailed pore-scale dynamics. Validated against prior methods and real-world imagery, our approach demonstrates enhanced physical accuracy and visual fidelity.

Our method has currently several limitations. First, we focus on high-porosity, fully saturable media. Our current approach also lacks anisotropic permeability support, cannot model reversible wetting effects, and is based on uniform viscosity assumptions in multiphase flow. In future work, we aim to explore anisotropic porous media, moisture loss effects on poroelasticity, and adaptive particle resolution for enhanced visual effects.

Table 3. Comparing Ren et al. [2021], Yan et al. [2016], and our method for simulating porous flow.

	Ren et al.	Yan et al	Ours
PEC mechanism modeling	×	×	✓
Incompressible porous flow	×	×	✓
Cavity-aware porous modeling	×	×	✓
Modular fluid-porous coupling	✓	×	✓
Conservation of mass	×	✓	✓
Support multiphase flow	✓	×	✓
Compare with Real-World Results	×	×	✓

Acknowledgments

This research is supported by National Science and Technology Major Project of the Ministry of Science and Technology of China (2024ZD0608100), National Natural Science Foundation of China (Nos.62376025, 62332017), Guangdong Basic and Applied Basic Research Foundation (No.2023A1515030177).

References

A Bedford and Do S Drumheller. 1983. Theories of immiscible and structured mixtures. *International Journal of Engineering Science* 21, 8 (1983), 863–960.

Jan Bender and Dan Koschier. 2016. Divergence-free SPH for incompressible and viscous fluids. *IEEE Transactions on Visualization and Computer Graphics* 23, 3 (2016), 1193–1206.

Wei Chen, Fei Zhu, Jing Zhao, Sheng Li, and Guoping Wang. 2018. Peridynamics-Based Fracture Animation for Elastoplastic Solids. In *Computer Graphics Forum*, Vol. 37. Wiley Online Library, 112–124.

Zhangxin Chen, Guanren Huan, and Yuanle Ma. 2006. *Computational methods for multiphase flows in porous media*. SIAM.

Cassidy J Curtis, Sean E Anderson, Joshua E Seims, Kurt W Fleischer, and David H Salesin. 1997. Computer-generated watercolor. In *Proceedings of the 24th annual conference on Computer graphics and interactive techniques*. 421–430.

Henry Philibert Gaspard Darcy. 1856. *Dètermination des lois d'ècoulement de l'eau à travers le sable*.

Brojeswari Das, A Das, VK Kothari, R Fangueiro, and M De Araújo. 2007. MOISTURE TRANSMISSION THROUGH TEXTILES: Part II: Evaluation Methods and Mathematical Modelling. *AUTEX Research Journal* 7, 3 (2007), 194–216.

Reint De Boer. 2012. *Theory of porous media: highlights in historical development and current state*. Springer Science & Business Media.

Sybren Ruurds de Groot and Peter Mazur. 1984. *Non-equilibrium Thermodynamics*. Courier Corporation.

Mengyuan Ding, Xuchen Han, Stephanie Wang, Theodore F Gast, and Joseph M Teran. 2019. A thermomechanical material point method for baking and cooking. *ACM Transactions on Graphics (TOG)* 38, 6 (2019), 1–14.

Yun Fei, Christopher Batty, Eitan Grinspun, and Changxi Zheng. 2018. A multi-scale model for simulating liquid-fabric interactions. *ACM Transactions on Graphics (TOG)* 37, 4 (2018), 1–16.

Adolf Fick. 1855. Ueber diffusion. *Annalen der physik* 170, 1 (1855), 59–86.

Ming Gao, Andre Pradhana, Xuchen Han, Qi Guo, Grant Kot, Eftychios Sifakis, and Chenfanfu Jiang. 2018. Animating fluid sediment mixture in particle-laden flows. *ACM Transactions on Graphics (TOG)* 37, 4 (2018), 1–11.

Jonghyun Ha and Ho-Young Kim. 2020. Capillarity in soft porous solids. *Annual Review of Fluid Mechanics* 52, 1 (2020), 263–284.

S Majid Hassanizadeh and William G Gray. 1990. Mechanics and thermodynamics of multiphase flow in porous media including interphase boundaries. *Advances in water resources* 13, 4 (1990), 169–186.

R Hilfer. 2006. Macroscopic capillarity and hysteresis for flow in porous media. *Physical Review E—Statistical, Nonlinear, and Soft Matter Physics* 73, 1 (2006), 016307.

Yuanming Hu, Tzu-Mao Li, Luke Anderson, Jonathan Ragan-Kelley, and Frédo Durand. 2019. Taichi: a language for high-performance computation on spatially sparse data structures. *ACM Transactions on Graphics (TOG)* 38, 6 (2019), 201.

Markus Huber, Simon Pabst, and Wolfgang Straßer. 2011. Wet cloth simulation. In *ACM SIGGRAPH 2011 Posters*. 1–1.

Markus Ihmsen, Jens Orthmann, Barbara Solenthaler, Andreas Kolb, and Matthias Teschner. 2014. SPH fluids in computer graphics. (2014).

Yuntao Jiang and Yingjie Lan. 2021. A Dynamic Mixture Model for Non-equilibrium Multiphase Fluids. In *Computer Graphics Forum*, Vol. 40. Wiley Online Library, 85–95.

Signe Kjelstrup, Dick Bedeaux, Alex Hansen, Bjørn Hafskjold, and Olav Galteland. 2018. Non-isothermal transport of multi-phase fluids in porous media. the entropy production. *Frontiers in Physics* 6 (2018), 126.

Toon Lenaerts, Bart Adams, and Philip Dutré. 2008. Porous flow in particle-based fluid simulations. *ACM Transactions on Graphics (TOG)* 27, 3 (2008), 1–8.

MoC Leverett. 1941. Capillary behavior in porous solids. *Transactions of the AIME* 142, 01 (1941), 152–169.

Ruolan Li. 2025. Source Code for: Multiphase Particle-Based Simulation of Poro-Elasto-Capillary Effects. https://github.com/dewiorchid/PEC_simulation.

Wei-Chin Lin. 2015. Boundary handling and porous flow for fluid–hair interactions. *Computers & Graphics* 52 (2015), 33–42.

Erdogan Madenci and Erkan Oterkus. 2014. *Peridynamic Theory*. Springer New York, New York, NY, 19–43.

Reza Masoodi and Krishna M Pillai. 2010. Darcy's law-based model for wicking in paper-like swelling porous media. *AIChE journal* 56, 9 (2010), 2257–2267.

Saket Patkar and Parag Chaudhuri. 2013. Wetting of porous solids. *IEEE transactions on visualization and computer graphics* 19, 9 (2013), 1592–1604.

Timo Probst and Matthias Teschner. 2024. Unified Pressure, Surface Tension and Friction for SPH Fluids. *ACM Transactions on Graphics* 44, 1 (2024), 1–28.

Bo Ren, Ben Xu, and Chenfeng Li. 2021. Unified particle system for multiple-fluid flow and porous material. *ACM Transactions on Graphics (TOG)* 40, 4 (2021), 1–14.

Witawat Rungjiratananon, Zoltan Szego, Yoshihiro Kanamori, and Tomoyuki Nishita. 2008. Real-time animation of sand-water interaction. In *Computer Graphics Forum*, Vol. 27. Wiley Online Library, 1887–1893.

David R Schuchard and John C Berg. 1991. Liquid transport in composite cellulose—superabsorbent fiber networks. *Wood and Fiber Science* (1991), 342–357.

Xin Shi and Shuangjiu Xiao. 2015. Fluid absorption and diffusion in and between porous materials. In *Proceedings of the 14th ACM SIGGRAPH International Conference on Virtual Reality Continuum and its Applications in Industry*. 23–26.

Dmitriy Silin and Tad Patzek. 2006. Pore space morphology analysis using maximal inscribed spheres. *Physica A: Statistical mechanics and its applications* 371, 2 (2006), 336–360.

Dmitry B Silin, Guodong Jin, and Tad W Patzek. 2003. Robust determination of the pore space morphology in sedimentary rocks. In *SPE Annual Technical Conference and Exhibition*. SPE, SPE–84296.

John C Slattery. 1969. Single-phase flow through porous media. *AIChE Journal* 15, 6 (1969), 866–872.

Haozhe Su, Siyu Zhang, Zherong Pan, Mridul Aanjaneya, Xifeng Gao, and Kui Wu. 2023. Real-time Height-field Simulation of Sand and Water Mixtures. In *SIGGRAPH Asia 2023 Conference Papers*. 1–10.

Thomas Sweijen, Ehsan Nikooee, S Majid Hassanizadeh, and Bruno Chareyre. 2016. The effects of swelling and porosity change on capillarity: DEM coupled with a pore-unit assembly method. *Transport in porous media* 113, 1 (2016), 207–226.

Andre Pradhana Tampubolon, Theodore Gast, Gergely Klár, Chuyuan Fu, Joseph Teran, Chenfanfu Jiang, and Ken Museth. 2017. Multi-species simulation of porous sand and water mixtures. *ACM Transactions on Graphics (TOG)* 36, 4 (2017), 1–11.

Pierre Van de Velde, Julien Dervaux, Camille Duprat, and Suzie Protière. 2023. Imbibition and collapse between swelling fibres. *Journal of Fluid Mechanics* 978 (2023).

Xiaokun Wang, Yanrui Xu, Sinuo Liu, Bo Ren, Jirí Kosinka, Alexandru C Telea, Jiamin Wang, Chongming Song, Jian Chang, Chenfeng Li, et al. 2024. Physics-based fluid simulation in computer graphics: Survey, research trends, and challenges. *Computational Visual Media* 10, 5 (2024), 803–858.

Edward W Washburn. 1921. The dynamics of capillary flow. *Physical review* 17, 3 (1921), 273.

Reinhard Woltmann. 1794. *Beitrage zur Hydraulischen architectur*. Vol. 3. Johann Christian Dieterich.

Yanrui Xu, Xiaokun Wang, Jiamin Wang, Chongming Song, Tiancheng Wang, Yalan Zhang, Jian Chang, Jian Jun Zhang, Jiri Kosinka, Alexandru Telea, et al. 2023. An implicitly stable mixture model for dynamic multi-fluid simulations. In *SIGGRAPH Asia 2023 Conference Papers*. 1–11.

Xiao Yan, Yun-Tao Jiang, Chen-Feng Li, Ralph R Martin, and Shi-Min Hu. 2016. Multiphase SPH simulation for interactive fluids and solids. *ACM Transactions on Graphics (TOG)* 35, 4 (2016), 1–11.

Yi Zheng, Lei Ma, Yanyun Chen, Guangzheng Fei, Bin Sheng, and Enhua Wu. 2020. Simulation of multi-solvent stains on textile. *The Visual Computer* 36 (2020), 2005–2016.

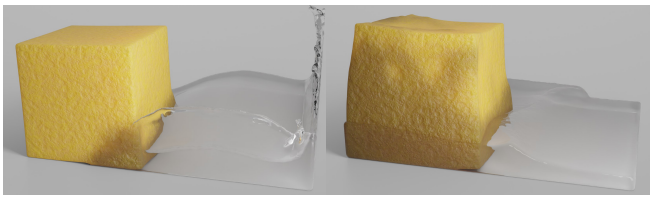

Fig. 5. A spongy porous medium absorbs water and swells.

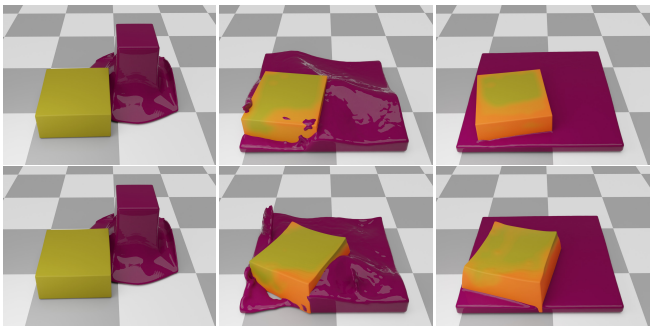

Fig. 6. Comparison of Poroelastic Swelling with [Ren et al. 2021]. (Top Row) Their original 'porous block absorption' experiment, reproduced for a direct comparison. (Bottom Row) Our method, under identical conditions, captures a more pronounced and realistic poroelastic swelling, evident in the block's volumetric expansion.

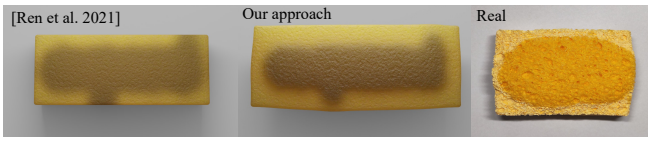

Fig. 7. Comparison of the post-wetting expansion in porous solids. Compared to [Ren et al. 2021], our method more closely matches the real-world fiber sponge expansion effect (right image), due to the swelling strain induced by internal wetting of the porous medium, resulting in an arc-shaped sponge outline.

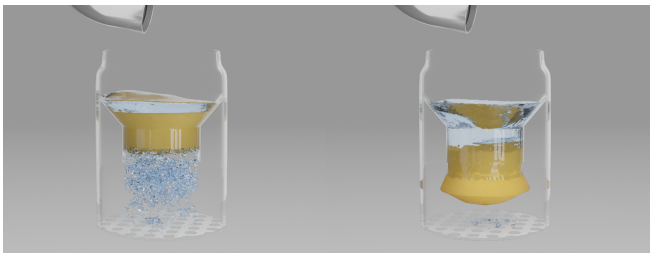

Fig. 8. Contrast in behavior: wetting softens the right plug, enabling it to pass through the funnel, while the left plug remains rigid.

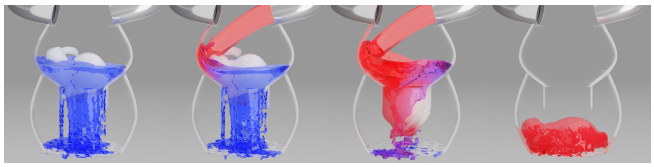

Fig. 9. Porous rabbit wetted by red phase, not blue, softens and passes through funnel. Circular holes in container base drain most blue fluid.

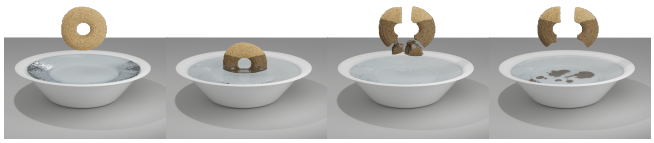

Fig. 10. A biscuit breaks after absorbing water. Note the different fracture behavior of the wetted and dry ends and the secondary breaking that occurs when the biscuit reaches the bottom of the bowl.

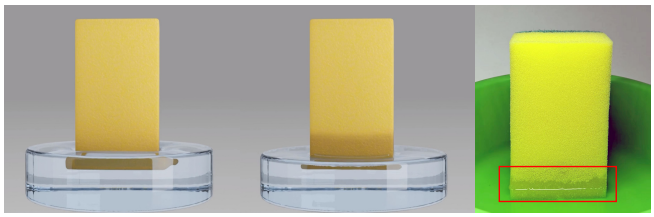

Fig. 11. A sponge imbibition experiment compares fluid intrusion into a porous medium. The left image shows [Yan et al. 2016]; the middle image shows our proposed method; the right image shows real-world results. Note the distinct boundary of fluid infiltration into the sponge, highlighted by the red box in the right image, which is also captured by our results.

Fig. 12. Following water absorption, the duck's weight increases, causing it to sink to the bottom. Note that our saturated porous medium exhibits a fully spontaneous mass increase process. In contrast, in [Ren et al. 2021], mass is artificially added to achieve a similar effect.

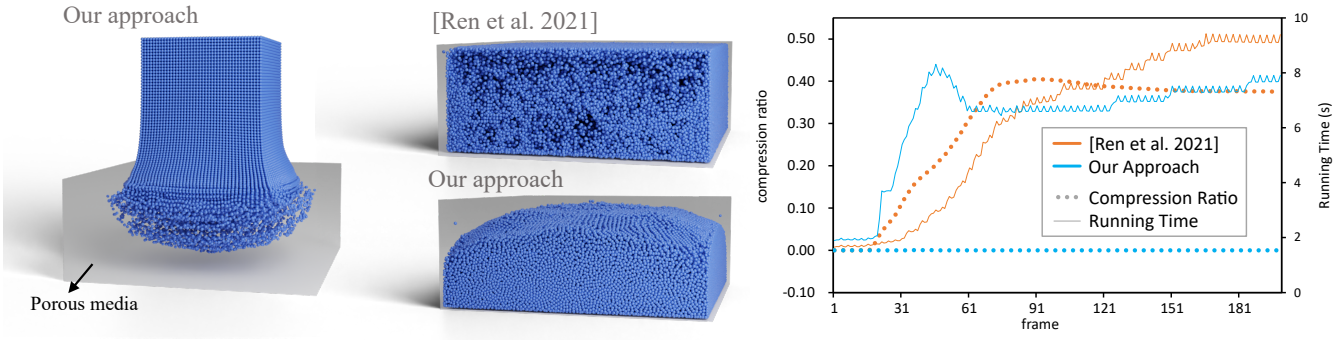

Fig. 13. Fluid compression and performance comparison. (Middle) Final particle distribution in the porous medium. (Right) The plot confirms our method's near-zero compression (dashed lines), unlike the significant compression in [Ren et al. 2021]. Performance-wise (solid lines), our method is initially slower but becomes more efficient as the simulation progresses.

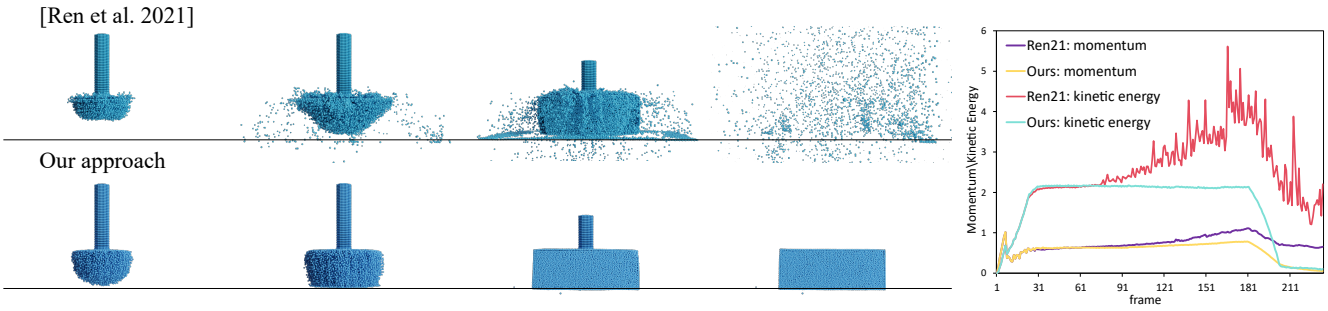

Fig. 14. Comparison of stability in a full saturation scenario. The visual sequence (left) shows our method maintains stability, while [Ren et al. 2021] suffers from fluid particle penetration at the boundaries. This is quantitatively confirmed by the energy and momentum plot (right). Our method's energy curve remains stable and converges to a steady state after injection ceases. In contrast, the energy curve for [Ren et al. 2021] exhibits abrupt oscillations and lacks final convergence, indicating a loss of stability. Note: the outer porous medium is not rendered to visualize the internal fluid.

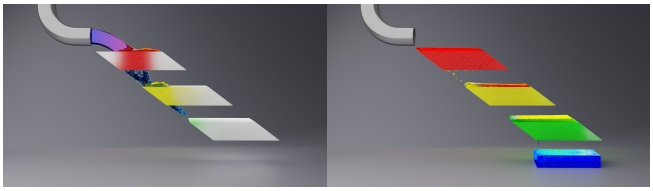

Fig. 15. After a four-phase fluid mixture is filtered through three layers of porous media, only the blue-phase fluid is retained. Due to the preset contact angles of each phase, differential permeability is observed.

Fig. 16. The sponge absorbs water to reach saturation. Next, a portion of the water is expelled by wringing out the sponge.

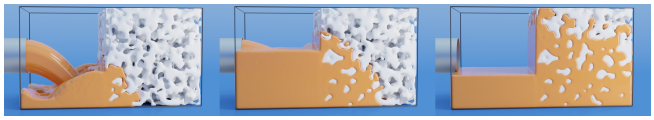

Fig. 17. Microscale simulation of capillary effects within a specific pore structure. Due to capillary action, the fluid counteracts gravity, nearly filling all cavities.